Draft version January 24, 2022
Typeset using LaTeX **twocolumn** style in AASTeX63

arXiv:1911.12398v1 [astro-ph.SR] 27 Nov 2019

Modeling the accretion disk around the high-mass protostar GGD 27-MM1

N. Añez-López,[1,2] M. Osorio,[3] G. Busquet,[1,2] J. M. Girart,[1,2] E. Macías,[4,5,6] C. Carrasco-González,[7] S. Curiel,[8] R. Estalella,[9] M. Fernández-López,[10] R. Galván-Madrid,[7] J. Kwon,[11] J.M. Torrelles,[1,2]

[1] *Institut de Ciències de l'Espai (ICE, CSIC), Can Magrans s/n, E-08193 Cerdanyola del Vallès, Catalonia*
[2] *Institut d'Estudis Espacials de Catalunya (IEEC), E-08034 Barcelona, Catalonia*
[3] *Instituto de Astrofísica de Andalucía (IAA, CSIC), Glorieta de la Astronomía s/n, E-18008 Granada, Spain*
[4] *Department of Astronomy, Boston University, 725 Commonwealth Avenue, Boston, MA 02215, USA*
[5] *Joint ALMA Observatory, Alonso de Córdova 3107, Vitacura, Santiago 763-0355, Chile*
[6] *European Southern Observatory, Alonso de Córdova 3107, Vitacura, Santiago 763-0355, Chile*
[7] *Instituto de Radioastronomía y Astrofísica (IRyA), UNAM, Apdo. Postal 72-3 (Xangari), Morelia, Michoacán 58089, México*
[8] *Instituto de Astronomía, Universidad Nacional Autónoma de México (UNAM), Apartado Postal 70-264, DF 04510 México*
[9] *Departament de Física Quàntica i Astrofísica, Institut de Ciències del Cosmos (ICC), Universitat de Barcelona (IEEC-UB), Martí i Franquès 1, 08028, Catalonia*
[10] *Instituto Argentino de Radioastronomía (CCT-La Plata, CONICET; CICPBA), C.C. No. 5, 1894, Villa Elisa, Buenos Aires, Argentina*
[11] *The University of Tokyo, Hongo 7-3-1, Bunkyo, Tokyo 113-0033, Japan*

ABSTRACT

Recent high-angular resolution ($\simeq$ 40 mas) ALMA observations at 1.14 mm resolve a compact ($R \simeq$ 200 au) flattened dust structure perpendicular to the HH 80–81 jet emanating from the GGD 27-MM1 high-mass protostar, making it a robust candidate for a true accretion disk. The jet/disk system (HH 80–81/GGD 27-MM1) resembles those found in association with low- and intermediate-mass protostars. We present radiative transfer models that fit the 1.14 mm ALMA dust image of this disk which allow us to obtain its physical parameters and predict its density and temperature structure. Our results indicate that this accretion disk is compact ($R_{\rm disk} \simeq$ 170 au) and massive ($\simeq 5\ M_\odot$), about 20% of the stellar mass of $\simeq 20\ M_\odot$. We estimate the total dynamical mass of the star-disk system from the molecular line emission finding a range between 21 and 30 $M_\odot$, which is consistent with our model. We fit the density and temperature structures found by our model with power law functions. These results suggest that accretion disks around massive stars are more massive and hotter than their low-mass siblings, but they still are quite stable. We also compare the temperature distribution in the GGD 27–MM1 disk with that found in low- and intermediate-mass stars and discuss possible implications on the water snow line. We have also carried out a study of the distance based on Gaia DR2 data and the population of young stellar objects (YSOs) in this region, and from the extinction maps. We conclude that the source distance is within 1.2 and 1.4 kpc, closer than what was derived in previous studies (1.7 kpc).

Keywords: stars: formation – ISM: individual objects (GGD 27, HH 80–81, IRAS 18162-2048) – stars: massive – protoplanetary disks

1. INTRODUCTION

Understanding how high-mass stars form and evolve is one of the hot topics in astrophysics, due to the strong impact that these objects have in the life of a galaxy. However, the study of high-mass protostars is difficult due to their fast evolution ($\sim 10^5$ yr) to the main sequence, their large distances and high obscuration.

It is well known that low-mass stars are formed through an accretion disk that transports gas and dust from the envelope to the protostar and through a jet that removes the excess of angular momentum (Shu, Lizano, & Adams 1987; McKee & Ostriker 2007). Disks around nearby solar-type stars have been studied to great extent and detail (e.g. Williams & Cieza 2011; Testi et al. 2014; Hartmann et al. 2016; Andrews et al. 2018), but at the moment the number of disks studies of more distant and massive stars is still comparatively very small.

Accretion disks around massive stars is a plausible mechanism that can alleviate the radiation pressure problem, hence allowing an accretion flow to continue once photo-ionization has started (e.g. Tan et al. 2014; Klassen et al. 2016; Kuiper & Hosokawa 2018). How-

ever, their physical properties are still uncertain (see e. g., Beltrán & de Wit 2016, for a recent review). Flattened, disk-like structures have been observed in a few massive young stars (Beltrán et al. 2011, 2014; Sánchez-Monge et al. 2014; Johnston et al. 2015; Sanna et al. 2018; Zapata et al. 2019). However, these structures are large ($\sim$ 1000–10000 au) and have masses considerably larger than the central protostar and it is difficult to envisage them as real accretion disks. Therefore higher angular resolution and more sensitivity observations are required to better characterize the physical parameters and the role of these rotating structures (e.g. Maud et al. 2019; Ginsburg et al. 2019). Three of the best examples in the literature of massive protostars associated with a clearly defined jet and a compact (few hundred au) angularly resolved dusty disk candidate are: Cepheus A HW2 (Patel et al. 2005), GGD 27-MM1 (Girart et al. 2018), and G11.92-061 MM1a (Ilee et al. 2018).

The HH 80–81 objects (at a distance of 1.4 kpc; see Appendix) are associated with a spectacular ($\sim$ 10 pc long) highly collimated radio-jet (Martí et al. 1993; Heathcote et al. 1998; Masqué et al. 2015), which is powered by a massive early B-type protostar IRAS 18162−2048 (GGD 27-MM1, Fernández-López et al. 2011a; Girart et al. 2017). This protostellar radio-jet is the first one where polarized emission due to relativistic electrons has been detected, showing the presence of a magnetic field aligned with the jet (Carrasco-González et al. 2010; Rodríguez-Kamenetzky et al. 2017). Very Large Array (VLA) continuum observations at 7 mm reveal a cross-shaped morphology which was interpreted as two overlapping structures that could correspond to the radio-jet and a disk of $\sim$200 au of radius (Carrasco-González et al. 2012), in agreement

with the upper limit imposed by the 1.3 mm continuum dust emission observations (Fernández-López et al. 2011a). The size of the putative disk coincides with theoretical predictions of the centrifugal radius based on the Spectral Energy Distribution (SED) fitting of some high-mass protostar regions (De Buizer, Osorio, & Calvet 2005).

In addition, observed velocity gradients in the molecular gas perpendicular to the HH80-81 radio jet have been interpreted as rotating motions (Fernández-López et al. 2011b; Carrasco-González et al. 2012; Girart et al. 2017). Definitive evidence of a compact disk around IRAS 18162-2048 comes from ALMA observations at 1.14 mm with an angular resolution of $\sim$ 40 mas ($\sim$ 56 au), which reveal a compact dust disk clearly perpendicular to the radio-jet (Girart et al. 2018, see Fig. 1).

Due to the similarities with disk-protostar-jet systems in low- and intermediate-mass protostars, in this paper we analyze the GGD 27–MM1 disk by applying models that have successfully explained disks around low-mass stars. The main goal is to investigate if the assumptions that are usually adopted for disks around low-mass stars can be roughly extrapolated to the case of massive stars. For example, disks around low-mass stars are much less massive than the central protostar and therefore they are usually gravitationally stable. In the high-mass case it is not clear if disks are stable (Maud et al. 2019) or unstable (Motogi et al. 2019; Zapata et al. 2019).

The paper layout is as follows. In Section 2 we present the ALMA observations of the disk around GGD 27–MM1, describing the disk model in Section 3. In Section 4 we present the main observational properties of the region. In Section 5 we explain the fit procedure and Sections 6 and 7 correspond to results and discussion, respectively. We list the main conclusions in Section 8 and present the new distance estimation in the Appendix.

2. ALMA OBSERVATIONS

In this work we use ALMA continuum observations at 1.14 mm (263.0 GHz; project ALMA#2015.1.00480.S). The Band 6 receiver with the correlator set in continuum mode (time division mode, TDM) covering the 253.0-257.0 GHz and 269.0-273.0 GHZ frequency ranges was used. The observations were carried out with 37 antennas in the c36-8/7 configuration, which provided baselines between 82 m and 11.05 km (13 to 5400 kλ). The Stokes I image toward GGD 27 -MM1 was generated using the resulting visibilities after the subtraction of the compact source (see Section 2.1). This was done using the CASA task *tclean* with a value of 0.5 for the robust Briggs weighting parameter. Because of a lack of visibilities between 150 and 300 kλ and in order to filter extended emission coming from the envelope, we used visibilities from baselines larger than 300 kλ (calibration of the data is described in Girart et al. 2018). The resulting synthesized beam has a full width at half maximum (FWHM) of 45.0 mas $\times$ 38.3 mas (PA = -62.4°). The Stokes I rms noise is 60 μJy beam^{-1}. The ALMA#2015.1.00480.S project had also a science goal at Band 7 to observe several molecular lines in the 298-302 and 310-313 GHz frequency ranges (c40-6 configuration). Here we analyze the position-velocity diagrams of two of the brightest lines detected that better trace the disk kinematics, SO_2 $9_{2,8}$–$8_{1,7}$ and $19_{3,17}$–$19_{2,18}$ transitions. For these two molecular lines, the calibrated data were self-calibrated from the continuum by using all the available channels in the four observed spectral windows, except for the channels with the brightest line emission (e.g., H_2CO $4_{2,3}$-$3_{1,2}$). Velocity channel maps were obtained (after continuum subtraction) using *tclean* with

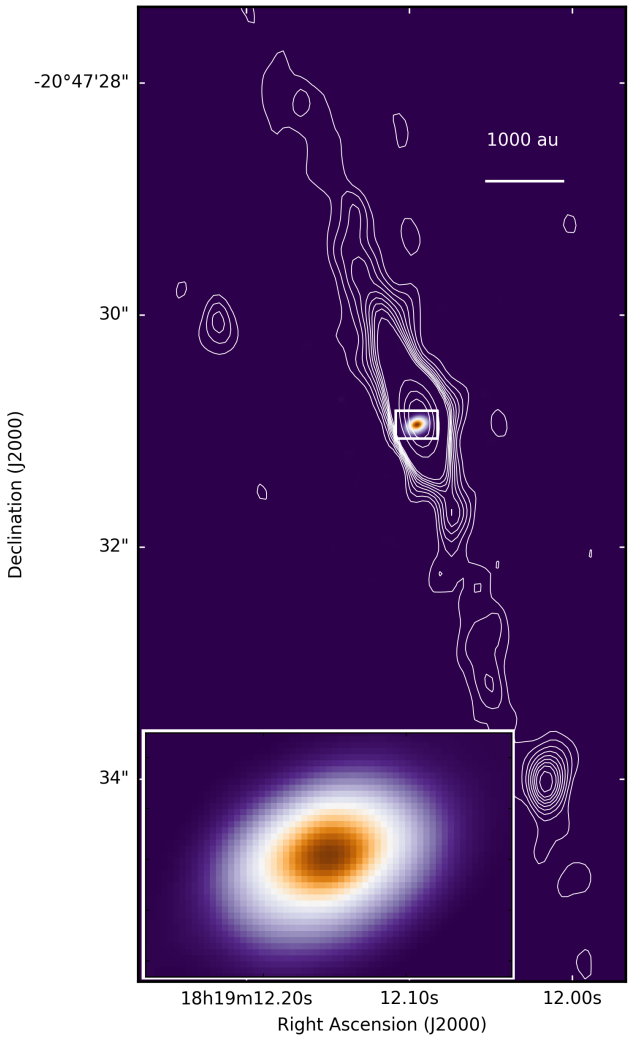


Figure 1. Disk and jet system of the massive star GGD 27 -MM1. The color image shows the dust continuum emission of the disk observed with ALMA at 1.14 mm with ∼40 mas angular resolution (∼56 au) (Girart et al. 2018, see also our Fig. 4). In contours it is shown the VLA image at 3.6 cm of the radio-jet observed with an angular resolution of ∼0.4 arcsec (Carrasco-González et al. 2012).

natural weighting, which yielded a FWHM synthesized beam of $0.21'' \times 0.16''$ (PA = $-87.1°$). The channel width was $\simeq$ 0.98 km s^{-1}. The rms noise achieved was 1.3 mJy beam^{-1} per channel. The other molecular lines detected will be presented in a forthcoming paper (Fernández-López et al. in prep.).

2.1. *The compact (few au) source at the disk center*

Figure 2 shows the real part of the observed visibilities as a function of the *uv* distance from the phase center (disk center). The flux density decreases steeply with increasing visibility radius, $r(u,v)$, for the shortest baselines ($r(u,v) \lesssim$ 2000 kλ). At larger radii the flux density decreases more smoothly up to $r(u,v) \simeq$4000 kλ. At this point the flux density remains roughly constant with the visibility radius. This suggests that the emission from the longest baselines may be dominated by a very compact object. To check this possibility, we generated several images using only visibilities with a minimum visibility radius, $r(u,v)_{\rm min}$, between 3500 and 4750 kλ and with a robust weighting of 1. The values of the minimum visibility radius used and the resulting synthesized beam are given in Table 1. Maps including only baselines longer than 4000 kλ are devoid of artifacts due to the severe missing flux density from the disk. The compact source appears in maps with long visibilities radii (see Fig. 3).

A two dimensional Gaussian fit was performed to the different images obtained with different baseline ranges. The flux density and the deconvolved size obtained from the Gaussian fit are listed in Table 1. The images with visibilities radii $\geq$ 4000 kλ show an unresolved source with a flux density of ∼19 mJy at the center of the disk. We also performed a Gaussian fit to the visibilities using the same range of visibilities as before. The flux density and size of these fits are also shown in Table 1. The fits to the visibilities with $r(u,v)_{\rm min}$>4000 and >4250 kλ reveal that the emission arises from a very compact region with a radius of $\sim$ 4 mas (∼5.6 au). Given the relatively short range of visibilities used in this fit, further very high angular resolution observations ($\sim$ 10 mas) are needed to better constrain its size. In any case, these values imply that the brightness temperature of this compact source is probably $\sim 10^4$ K.

The origin of the compact source cannot be due to the thermal emission of dust grains but rather to ionized gas (see Section 7.1). Therefore, this compact source was removed from the visibilities to obtain the map presented here, tracing only the dust emission from the accretion disk (Fig. 4).

3. DISK MODEL

The disk was modeled using the irradiated α-accretion disk models created by D'Alessio et al. (1998, 1999, 2001, 2006), which have been successfully used and further developed to model disks around low- and intermediate-mass stars (e.g.; McClure et al. 2013; Osorio et al. 2014, 2016; Macías et al. 2018).

The models describe disks around stars with parameters typical of classical T Tauris; that is, an irradiated flared disk with two population of grains. These two populations aim at emulating the dust growth and vertical settling predicted by dust evolution models (Dullemond & Dominik 2004). The code computes the vertical and the radial structure of the disk using the α-

Table 1. Gaussian fit to the Compact Source

	Image plane			Visibility plane	
$r(u,v)_{\rm min}$	Synthesized Beam	Flux density	Deconvolved Size	Flux density	Size
(kλ)	(mas×mas,°)	(mJy)	(mas×mas,°)	(mJy)	(mas)
3500	26.7×22.4, -63	28.5±0.2	16±1×7±1, 91±5	29.5±0.1	13.6±0.1
4000	23.8×20.9, -68	21.0±0.2	unresolved	20.8±0.1	4.7±0.5
4250	21.9×20.9, -59	20.1±0.2	unresolved	19.9±0.3	3.5±1.0
4500	21.6×19.8, 77	19.7±0.3	unresolved	19.3±0.4	failed [a]
4750	21.8×18.3, 67	19.1±0.4	unresolved	19.5±0.6	failed [a]

[a] Algorithm did not found solution probably due to the small range of visibilities.

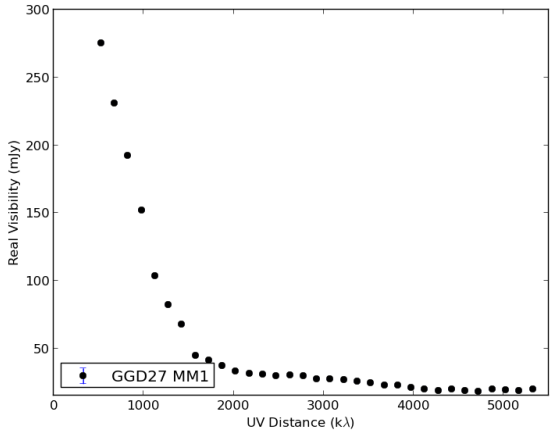


Figure 2. Annular average of the real part of the 1.14 mm ALMA visibilities, centered in GGD 27 MM1, as a function of the *uv* distance where the error bars are smaller than symbols.

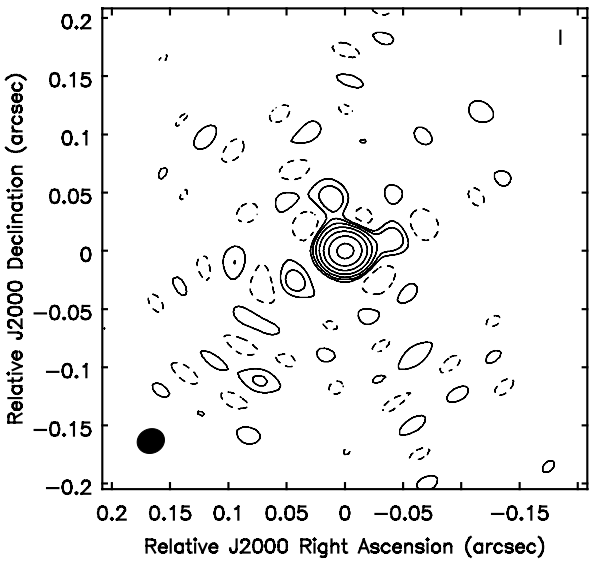


Figure 3. 1.14 mm ALMA image of GGD 27 MM1 obtained using only visibilities from baselines larger than ≥4000 kλ. Contour levels start at 4–σ, where σ is 0.06 mJy beam^{-1}, and then increase by a factor two at each contour. The emission shows a compact source with a brightness temperature ∼10^4K, likely associated with free-free emission (see Section 7.1).

viscosity prescription and enforcing vertical hydrostatic equilibrium. In the past, these models have already been used to reproduce the spectral energy distribution (SED) of a possible disk around the high-mass protostar AFGL 2591-VLA 3 (Trinidad et al. 2003). Furthermore, the α-viscosity prescription has been also used to model quasi-steady selfgravitating disks around massive protostars under certain conditions ($H/R \leq 0.1$ and $M_{\rm disk}/M_* < 0.5$, with H the disk scale height, and R the radius of the disk; Forgan et al. 2016).

The model allows to set two populations of grains, with a power-law size distribution $n(a) \propto a^{-3.5}$, where a is the grain radius. Regarding the degree of settling, we used the epsilon parameter $\epsilon = \zeta_{\rm small}/\zeta_{\rm std}$, where $\zeta_{\rm small}$ and $\zeta_{\rm std}$ are the dust-to-gas mass ratio of the small grains and the initial standard value respectively (see D'Alessio et al. 2006). The relative abundances of the different dust components were adopted with a dust-to-gas ratio of 0.0065 corresponding to the measured abundances of silicates and graphites in the ISM (Draine & Lee 1984; D'Alessio et al. 2006; Osorio et al. 2014). The remaining ratio up to the commonly used value of 0.01 would be water ice and other ices. These ices sould be sublimated at the high temperatures expected in the disk, so they should have a negligible contribution in the model (see Section 7.6.)

Other parameter related with the settling is $Z_{\rm big}$ that locates, as a function of the scale height (H), the border between both populations of grains, which was fixed as $Z_{\rm big}$=0.1H.

The main heating sources are the stellar irradiation and the viscous dissipation, which is parameterized

through α (Shakura & Sunyaev 1973) and it is assumed to be constant over the disk. The viscosity effective coefficient is defined as $\nu_t = \alpha c_s H$, where c_s is the local sound speed, and H is the hydrostatic scale height of the gas:

$$\frac{H}{R} = \frac{c_s(T_c)}{R\Omega(R)} = \left[\frac{kT_c R}{GM_{tot}\mu m_H}\right]^{1/2}, \quad (1)$$

where k is the Boltzmann constant, T_c is the disk mid-plane temperature, G is the gravitational constant, M_{tot} is the total mass ($M_* + M_{disk}$) at every radius, μ=2.33 is the mean molecular weight and m_H is the hydrogen mass. Besides, the model considers accretion luminosity as part of the irradiation of the disk.

The temperature and density structure are calculated self-consistently once the stellar parameters (radius R_*, mass M_*, and temperature T_*), the dust content (abundances, distribution of grain sizes), viscosity (α), and disk mass accretion rate ($\dot{M}_{acc}$) are set. The dust opacity includes absorption and isotropic self-scattering. In an α-accretion disk model the mass surface density is $\Sigma = \dot{M}_{acc}\Omega/3\pi\alpha c_s(T_c)^2$. The remaining parameters to describe the disk model are: the disk radius, R_{disk}, and the inclination angle of the disk i.

The disk is considered to be steady, axisymmetric, and geometrically thin. Its self-gravity is neglected compared to the stellar gravity, and it is assumed to be in Keplerian rotation and in hydrostatic equilibrium in the vertical direction. The model assumes that dust and gas are well mixed and thermally coupled; thus, a unique temperature as a function of position in the disk is calculated.

4. THE GGD 27-MM1 DISK-JET SYSTEM

In this section we present the main observational properties that can be used to constrain the parameters of our disk model. Figure 4 shows the ALMA continuum image of the GGD 27–MM1 disk at 1.14 mm. We resolve the disk at this wavelength, obtaining a flux density of 351.30 ± 0.33 mJy and a peak intensity of 46 mJy beam^{-1} (see also Busquet et al. 2019). The morphology observed at this wavelength is consistent with an inclined disk (49°; 0° for a face-on disk) with a radius of ∼ 240 au and PA= 113°. The brightness temperatures of the disk in the central region reaches a value of ∼ 470 K (Girart et al. 2018). This is an indication of an important source of heating.

Although there are not enough data points at different frequencies with high angular resolution to build the SED of the disk, we have extensive knowledge of the region that provides us with a series of observational constraints regarding the physical parameters of our model, which are discussed below.

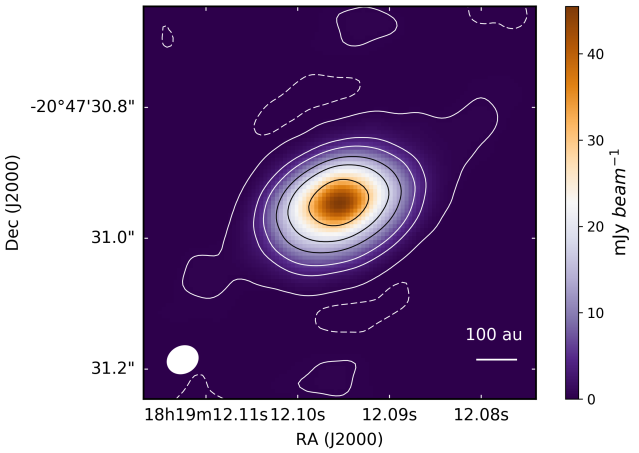


Figure 4. ALMA image at 1.14 mm of the GGD 27-MM1 disk. The contour levels are -5, 5, 50, 100, 200, 300, 500 times the rms noise (0.06 mJy beam^{-1}). The conversion factor from flux density to brightness temperature is ∼8.9 K mJy^{-1} beam.

Bolometric luminosity. The observed value is ∼2.0 ×10^4 $L_\odot$ for a distance of 1.7 kpc (Gómez et al. 2003). As shown in the appendix the source distance is between 1.2 and 1.4 kpc, and therefore the luminosity can be recalculated to be between ∼1.0 ×10^4 and ∼1.4 × 10^4 $L_\odot$. This luminosity must be considered an upper limit for the massive protostar GGD 27–MM1 since it comes mainly from the IRAS fluxes that probably encompasses other sources (Fernández-López et al. 2011a).

Dynamical mass. The total dynamical mass of the star-disk system can be obtained from the molecular line emission tracing the gas motions from the disk and assuming that they behave as a rotationally-supported disk (i.e., Keplerian velocity). We used the data cubes for the SO_2 $9_{2,8}$–$8_{1,7}$ and $19_{3,17}$–$19_{2,18}$ lines (see Section 2) to construct position-velocity (PV) maps, centered at the dust peak intensity with a position angle of 113°, i.e. along the major axis of the disk. Figure 5 shows the resulting plots. The brightest blueshifted emission appears in the south-east side of the disk, while the redshifted emission arises from the north-west side of the disk. This is in agreement with previous lower angular resolution and less sensitive observations (Fernández-López et al. 2011b; Carrasco-González et al. 2012; Girart et al. 2017). We note that there is also significant red/blueshifted emission in the SW/NE side of the disk. This could be an indication of infall motions, although MHD simulation of disk formation and evolution shows that this can be also a projection effect for significant inclinations (e.g., Seifried et al. 2016). In order to constrain the dynamical mass from these PV maps, we followed the procedure given by Seifried et al. (2016). This procedure fits the Keplerian profile to the 5-σ contour

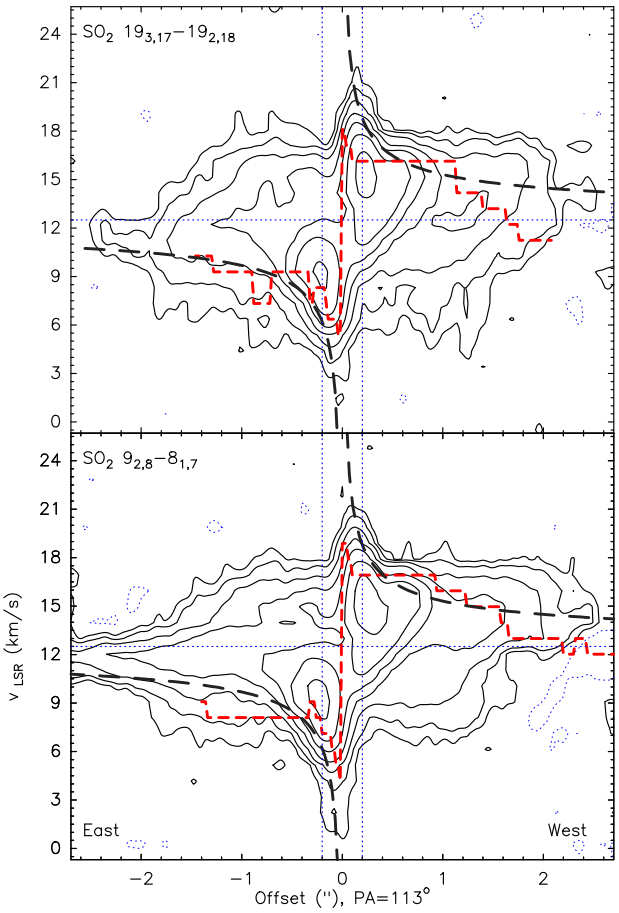


Figure 5. Position-velocity plots along the major axis of the disk for the SO_2 $9_{2,8}$–$8_{1,7}$ and $19_{3,17}$–$19_{2,18}$ lines. Contours are 2, 4, 8, 16, 32, 64 and 128 times the rms noise of the maps, 1.2 mJy beam^{-1}. The dashed black line shows the expected Keplerian profile for a 25 $M_\odot$. The red dashed line shows the best Keplerian fit to the data using the method proposed by Seifried et al. (2016) at 5-σ. The fit corresponds to a dynamical mass of 30 and 21 $M_\odot$ for SO_2 $9_{2,8}$–$8_{1,7}$ and $19_{3,17}$–$19_{2,18}$ lines, respectively.

emission, and was tested in synthetic ALMA molecular line PV maps generated from MHD simulations for disks around both low- and high-mass stars. It should best work for lines that fully resolve, spatially and kinematically, the Keplerian profile in the PV maps and for cases not too close to a face-on projection. The best fit obtained yielded an inclination corrected dynamical mass of 31±1 and 21±1 $M_\odot$ for the SO_2 $9_{2,8}$–$8_{1,7}$ and $19_{3,17}$–$19_{2,18}$ lines, respectively. Since the line emission mostly arises from the outskirts of the dusty disk modelled in this paper, we can consider this dynamical mass as the combined mass of the star and the accretion disk. Thus we explored stellar mass values between 15 and 25 $M_\odot$ and keep the total mass (star + disk) close to the dynamical mass.

Mass accretion rate. Carrasco-González et al. (2012) estimate the mass-loss rate in the jet using the formulation given by Reynolds (1986) (see Eq. 2), who model the free-free emission from an ionized jet adopting a power-law dependence with radius (see also Anglada et al. 2018):

$$\left[\frac{\dot{M}_{out}}{M_\odot yr^{-1}}\right] = 1.9\times10^{-6} x_0^{-1} \left[\frac{v_{jet}}{1000 kms^{-1}}\right] \left[\frac{S_\nu}{mJy}\right]^{0.75} \times \left[\frac{\nu}{GHz}\right]^{-0.45} \left[\frac{D}{kpc}\right]^{1.5} \left[\frac{\theta_0}{rad}\right]^{0.75} \quad (2)$$

they assume a pure hydrogen jet with constant opening angle $\theta_0 \sim 19°$ (conical jet), terminal velocity $v_{\rm jet}$ ($\sim$ 1000 km s^{-1}), ionization fraction $x_0 = 0.1$, electron temperature $T_{\rm e}$=10^4 K, and that the jet axis is in the plane of the sky. They obtain a mass-loss rate of $\dot{M}_{\rm out}$ $\sim10^{-5}$ $M_\odot$ yr^{-1} for a distance of 1.7 kpc, $\simeq 8\times10^{-6}$ $M_\odot$ yr^{-1} for the corrected distance of 1.4 kpc (see appendix). This value is in agreement with the value obtained from CO observations of the molecular outflow associated with the jet (Qiu et al. 2019). Assuming the accretion rate $\dot{M}_{\rm acc}$ of the disk onto the star to be $\sim$10 times larger than the mass-loss rate (Bontemps et al. 1996), the mass accretion rate would be $\dot{M}_{\rm acc}\sim 8\times10^{-5}$ $M_\odot$ yr^{-1}. However, Beltrán & de Wit (2016) (and references therein), obtain a ratio between the mass-loss rate and mass-accretion rate of approximately $\sim$0.3 for disks in young high-mass stars. In this case the mass accretion rate would be lower, $\sim 3\times10^{-5}$ $M_\odot$ yr^{-1}.

Even though the mass accretion rate is not well determined using these methods, it allows to define a range of values to explore. Therefore, in our modeling we explored values of $\dot{M}_{\rm acc}$ in the $\sim 1\times10^{-5}$ to $\sim 2\times10^{-4}$ $M_\odot$ yr^{-1} range.

Stellar parameters. It is expected that most of the dynamical mass (21-31 $M_\odot$) is stellar, otherwise the disk would be unstable and would show significant asymmetries (e.g., spiral structures) that are not observed with the present data. Such massive star, if it were in the main sequence, should develop an H II region, which is not detected with the present observations (see Sect. 7.1). A possible solution to mitigate this problem is to assume that the star is inflated, with low enough temperature for not producing stellar UV radiation and create an H II region.

In that sense, Hosokawa & Omukai (2009) found a dependence of the protostellar radius with the accretion rate. They obtain that, in general, the higher is the accretion rate, the larger is the stellar radius. Then the protostar has a lower maximum temperature for a certain stellar mass. This fact causes a delay in the onset of the main sequence phase and therefore a delay

in the formation of an H II region. Thus, because of the high accretion rate estimated, we decided to explore large stellar radii, between 10 and 30 $R_\odot$. Because the luminosity is known, this implies temperatures between 12000 and 18000 K. This is consistent with Johnston et al. (2013), who modeled the envelope and disk around the luminous star AFGL 2591-VLA3 (2.3 $\times 10^5$ $L_\odot$), and find a stellar radius of 90 $R_\odot$ with a temperature of 13000 K.

Inner disk radius. Considering a sublimation temperature of 1400 K for the most refractory grains (D'Alessio et al. 2006) and the observed luminosity, we can locate the sublimation wall from $L_{\rm tot} = 4\pi\sigma T^4 R^2$ at ~ 12 au of radius. Because of the high spatial resolution of the observations (~ 56 au), an inner radius larger than ~ 20 au was discarded. Otherwise we should marginally resolve the inner wall of the disk. The sublimation temperature usually is assumed to cover a range from 1200-1500 K, thus we explored an inner radius range between 10 and 20 au instead to just using the 12 au that we calculated (see Table 2).

Settling degree and grain size. We can obtain some constraints about the settling of the larger dust grain at the mid-plane looking at the polarization emission due to scattering from large grains. Based on polarization observations, Girart et al. (2018) do not find signs of dust settling, and determine a dust maximum grain size (a_{max}) from 50 to 500 μm (see Section 7.2). We explored in our modeling cases with different settling degree, including the no settling case.

Taking into account the observational restrictions set out above, in the following we proceed to look for the set of parameters that best fit the observations.

5. THE MODEL-FITTING PROCEDURE

We computed several grids of models varying the parameters of the disk and the star. Through these grids the parameters were refined until the best-fit model image.

The fitting procedure and analysis was done using Common Astronomy Software Applications (CASA) and Multichannel Image Reconstruction, Image Analysis, and Display (MIRIAD; Sault et al. 1995) data reduction software packages.

In order to properly compare the model with the ALMA data, synthetic visibilities were computed from the model images. This was done with the CASA *simutil* package. After that, *tclean* of CASA was used with the simulated visibilities to create a final image from the model adopting the same cleaning parameters used to create the observed ALMA image. In Fig. 6 we show the ALMA image (top panel), the modelled image (middle panel), and the residual map (bottom panel). The residual map was obtained by subtracting the model image from the observed one. Therefore positive values in the residuals show regions where the model underestimates the emission.

Table 2. Explored parameters range

Parameter	Values	Step
Star mass ($M_\odot$)	15 – 25	1
Temp. eff. (K)	12000 – 18000	1000
Star radius ($R_\odot$)	10 – 30	5
Acc. rate ($M_\odot$ yr^{-1})	1×10^{-5}– 2×10^{-4}	1×10^{-5}
Disk radius (au)	130 – 250	10
Inner radius (au)	10 – 20	1
Inclination(degrees)	44 – 54	1
a_{max} (μm)	100, 500 and 1000	-
α	0.1, 0.01 and 0.001	-

The radial intensity profile was computed averaging in concentric ellipses every 0.″01 ($\sim 1/4$ of the beam) with the inclination adopted in the disk model (see Fig. 7). The best fit parameters of the disk model were obtained initially by visual inspection of the radial intensity profile and then, from among this first selection we chose the best fit model based on minimum χ^2 of the residual map. In the case of the residual map, only pixels inside of ellipse with R=230 au were considered to calculate the χ^2 (see Fig. 4) to avoid contamination from the outskirts of the map. Appendix B shows the variation of the disk parameters with χ^2 (leaving the other parameters fixed).

6. RESULTS

In this section we present the best fit model obtained after exploring a wide range of values in the space of parameters of the model presented in Section 3. The best fit parameters are shown in Table 3.

We found a massive disk of ~ 5 $M_\odot$, i.e. 20% of the stellar mass. The radius of the disk is ~ 170 au with an inclination angle of $\sim 49°$ (angle between the rotation axis and the line of sight). The mass accretion rate, which in our model is a very sensitive parameter, resulted to be ~ 7 $\times 10^{-5}$ $M_\odot$ yr^{-1}. The total luminosity is $\sim 1\times 10^4$ $L_\odot$ which is in agreement with the previous estimation (see Section 4). The stellar mass is 20 $M_\odot$ which together with disk mass (5 $M_\odot$), is consistent with the estimated dynamical mass for the star-disk system (21–30 $M_\odot$; see Section 4).

Table 3. Best fit model parameters

Parameter	Value	
$M_*(M_\odot)$	20	fitted
$T_{\rm eff}$ (K)	12000	fitted
R_* ($R_\odot$)	25	fitted
Distance (kpc)	1.4	adopted
$\dot{M}$ ($M_\odot$ yr^{-1})	7×10^{-5}	adopted/refined [a]
$M_{\rm disk}$ ($M_\odot$)	5	calculated
$R_{\rm disk}$ (au)	168	adopted/refined [a]
H_{100} (au)	7	calculated
$R_{\rm in}$ (au)	14	fitted
i (degree)	49	adopted/refined [a]
a_{max} (μm)	500	fitted
α	0.1	fitted

[a]Parameter with observational constrains and uncertainty.

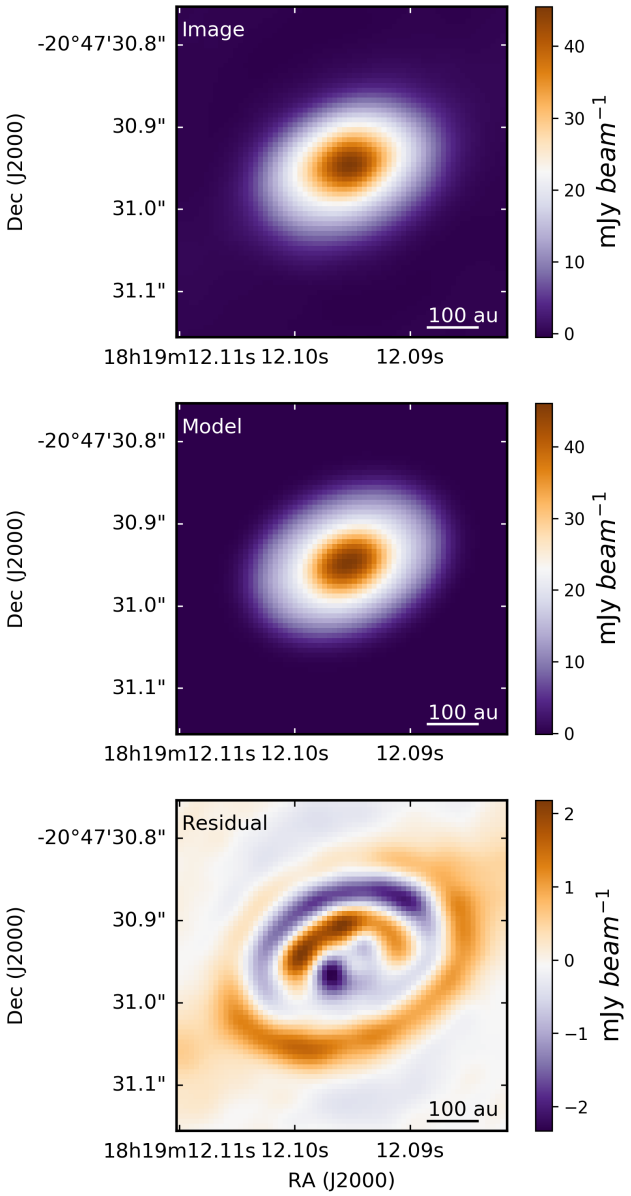


Figure 6. Observed ALMA 1.14 mm image (top panel), best fit disk model (middle plane), and the residual (image−model) map (bottom panel). The conversion factor from flux density to brightness temperature is ∼8.9 K mJy^{-1} beam.

Regarding the composition of the disk in terms of grain size, different maximum size of grains according with results found in Girart et al. (2018) were tested (see Section 4). We did not find substantial differences between models with a_{max} of 100, 500 μm and with 1 mm (see Fig. 8). Only for small radii (< 0.05") the difference between the models is noticeable. The grain sizes of the best fit model goes from a minimum value of 0.005 μm to a maximum of 3 μm in the disk upper layer. For those grains settled in the disk mid-plane the grain sizes are between 5 μm and 500 μm.

The density and temperature profiles for the best fit model are shown in Fig. 9. We found a flared disk with a maximum scale height of ∼13 au. The disk shows a temperature profile that goes from ∼1400 K at the inner edge of the disk to ∼150 K at the outer part. The small irregularities that can be seen in the internal part of the disk are caused by numerical effects and by the sublimation of the different dust components, which result in a step in the dust opacity, but they do not affect the results.

From the mass surface density (Σ) and using the total opacity of the model (absorption + self-scattering), $\chi = 0.13$ cm^2/g (opacity for a dust grain mixture with the physical properties described in Section 3 and with a grain size distribution which assumes grains with a maximum radius of 500 μm and considers the scattering effects), we obtain an optically thick disk at 1.14 mm for all radii, with $\tau = \Sigma\chi$ ranging from 50 to 170. In Busquet et al. (2019) they computed the mass of gas and dust of the disk assuming that the 1.14 mm dust continuum emission is optically thin and the temperature distribution is uniform ($T_{\rm d}$=109 K). They estimated a disk mass for GGD 27 MM1 of ∼0.5 $M_\odot$. This mass could be considered as a lower limit due to the optical thickness of the disk and to the fact that the opacity due to the self-scattering is not considered. We fitted the density and the temperature profiles with a power law functions ($\Sigma(R) \propto R^p$, $T(R) \propto R^q$) using the method of the minimum mean squared error (MSE). Here we

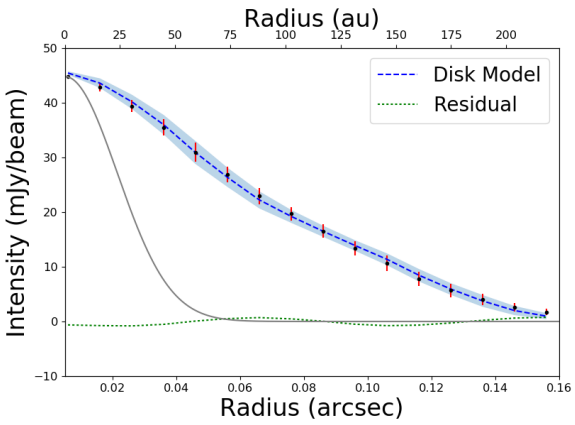


Figure 7. Averaged radial intensity profile at 1.14 mm. Dots represent the averaged value at each radius for the observed image and error bars represent the standard deviation. The blue dashed line is the averaged value at each radius for the disk model and the blue shadow is the standard deviation. The grey line depicts the synthesized beam of the ALMA observations. The dotted green line indicates the residual (difference between observed and modeled profile).

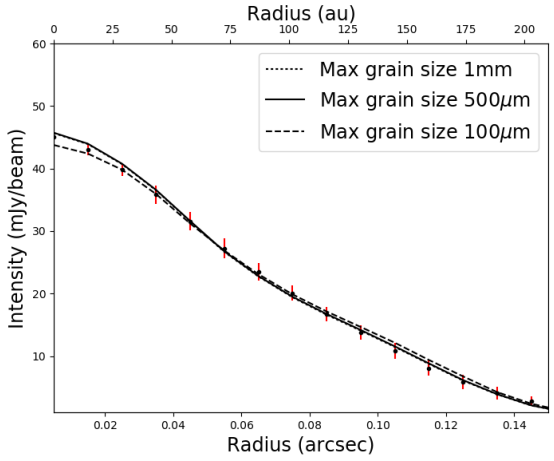


Figure 8. Radial intensity profile for three models with the same parameters given in Table 3, except a_{max} of 100 μm, 500 μm, and 1 mm.

present the coefficient and the power index. Equations 3 show the behaviour of the surface density, $\Sigma(R)$, and the temperature at the mid-plane, $T_c(R)$, approximated as power laws. The MSE of the fits are 0.023, and 0.034 respectively.

$$\begin{aligned} \frac{\Sigma(R)}{[\mathrm{g/cm^2}]} &\sim 500 \left(\frac{R}{[100\ \mathrm{au}]}\right)^{-0.5} \\ \frac{T_c(R)}{[\mathrm{K}]} &\sim 300 \left(\frac{R}{[100\ \mathrm{au}]}\right)^{-1} \end{aligned} \tag{3}$$

7. DISCUSSION

In this work we have studied the ALMA image at 1.14 mm of the circumstellar disk around GGD 27 - MM1. We found a compact source coming from the inner radius ($\sim$ 4 mas/5.6 au) probably due to ionized gas. By modeling the dust continuum emission from the disk (with the compact source previously subtracted), we found a massive ($\sim$ 5 $M_\odot$) and compact ($\sim$ 170 au) disk. In the following we discuss the implications of our results, while also analyzing the gravitational stability of the disk.

7.1. *Ionized component*

The compact source reported in Sect. 2.1 appears unresolved in the different images obtained with a minimum visibility radius of 4000 kλ (Fig. 3). The Gaussian fits in the visibility domain indicate that the source has a radius of $\sim$5.6 au and a brightness temperature of $\sim 10^4$ K. At such high temperature, the dust grains should be sublimated. Indeed, the expected temperature for the sublimation of silicates is $\sim$1400 K (D'Alessio et al. 2006). Therefore, the most plausible explanation is that this compact emission is tracing ionized gas, either from an incipient and extremely compact H II region or from the base of the HH 80–81 thermal radio-jet, best traced at cm-wavelengths (e.g., Carrasco-González et al. 2012). In fact, from the peak flux density measured at 1.3 cm at the center of the radio-jet ($\sim$1 mJy; Carrasco-González et al. 2012), and the flux density measured at 1.14 mm $\sim$19 mJy (see Sec. 2.1), we estimated a spectral index of α $\sim$1.2 between these two frequencies. This value is within the range of spectral indices measured in thermal radio-jets associated with YSOs (e.g., Anglada et al. 2018). Higher resolution and multi-frequency observations would help determine the nature of this compact component in a conclusive way.

7.2. *Restrictions from polarization*

An important source of information about the composition of the disks in terms of grain size, grain shape, and grain distribution comes from polarimetric observation.

Polarization data allows to constrain the dust distribution in the disk (settling) and the maximum dust grain size. Girart et al. (2018) based on polarization models of Yang et al. (2017) conclude that dust settling has not yet occurred . Yang et al. (2017) compare two models with different thickness of the layer of large grains which are responsible for the scattering, and propose two models in which large grains can be found up to 0.1 H' and 1 H', where H' is the (dust) hydrostatic scale height, $H'(R) = H'_0(R/R_c)^{1.5-q/2}$ being R_c a characteristic radius of the disk (dust) density distribution, and q the temperature power law index.

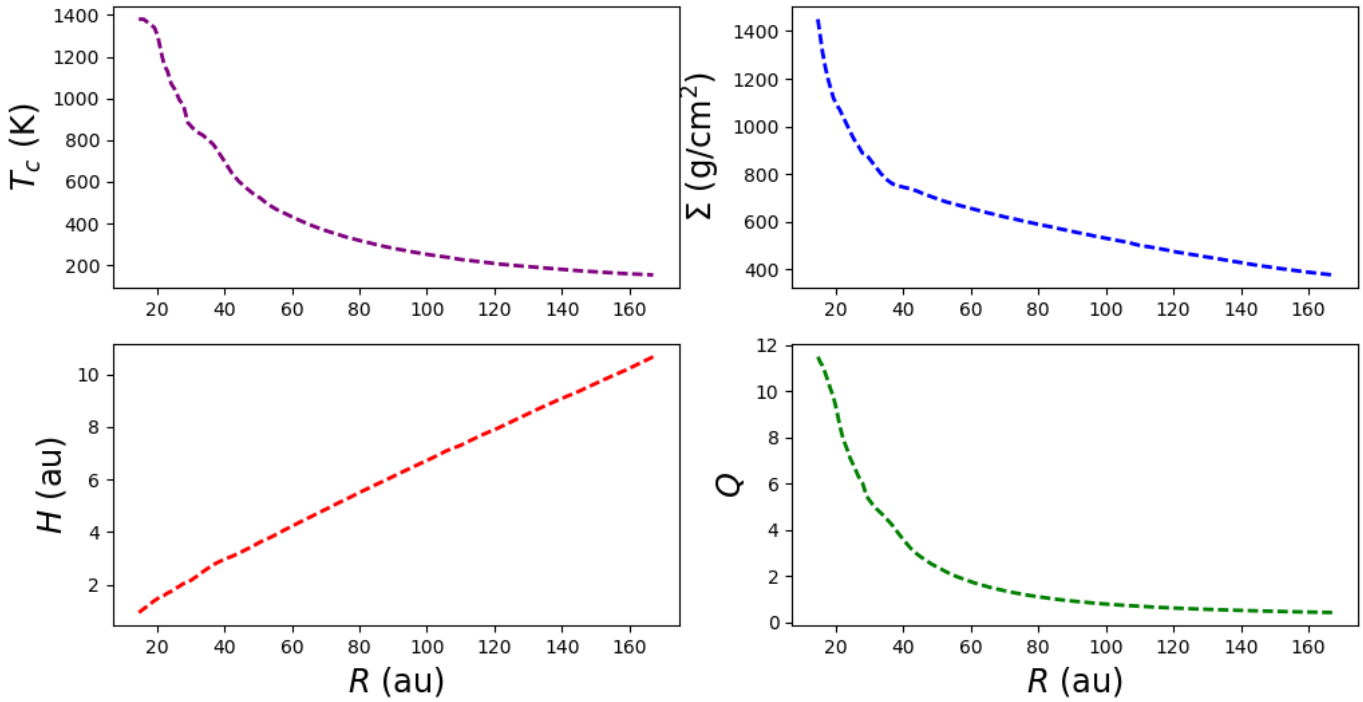


Figure 9. *Upper*: Temperature at the mid-plane (left) and surface density (right). *Bottom*: Scale height, H (left) and Toomre parameter Q, see Section 7.3 (right).

Unlike the models of these authors, our models consider the dust settling changing the dust-to-gas mass ratio between two populations through the ϵ parameter as explained in Section 3. Small grains are in the upper layer and big grains are in the mid-plane. The position of the border between these two populations can be set through the parameter $Z_{\rm big}$.

In this work our best fit model has ϵ=1 (no dust settling) but it still has two dust populations with the border located at $Z_{\rm big}$=0.1H, where H is the pressure scale height of the gas at the mid-plane temperature (see Section 3).

We also reproduced the scenario suggested by Yang et al. (2017) to reproduce the polarization pattern observed by Girart et al. (2018). To do so, we tested a model with Z$_{\rm big}$ =1 H and ϵ =1. In this case we obtained a more massive disk (7 $M_\odot$) with larger mass accretion rate (1×10^{-4} $M_\odot$ yr^{-1}) than the model with $Z_{\rm big}$=0.1H ($M_{\rm disk} \sim 5$ $M_\odot$ and $\dot{M}_{\rm acc} \sim 7 \times 10^{-5}$ $M_\odot$ yr^{-1}; see Table 3), our fiducial best fit model, which shows a lower value of χ^2.

Furthermore, we have compared two- and one-population models. We tested models with a single dust grain population with a maximum grain size of 500 μm. Due to the lower opacity to the stellar radiation of this dust population, the one-population models would require significantly higher disk masses, even comparable to the stellar mass. These masses are inconsistent with our estimated dynamical mass (see Section 4, indicating that at least two dust populations are needed to fit the observations.

In summary, we have considered the results presented in Girart et al. (2018) concerning the size and distribution of grains. Moreover, taking into account the conceptual differences presented above (H, H'), we have explored values adjacent to them. We did not find substantial differences between both scenarios and therefore we can not favor either.

7.3. *Stability of the disk*

We have quantified the Toomre parameter of our model to check the stability of the disk against self-gravity perturbations. Figure 9 (bottom right) shows the Toomre parameter Q (Eq. 4) for a Keplerian disk evaluated at the disk mid-plane temperature.

$$\begin{aligned} Q &= \frac{c_s \Omega}{\pi G \Sigma} \\ \Omega &= \left(\frac{G M_{total}}{R^3}\right)^{1/2}, \end{aligned} \tag{4}$$

where c_s is the sound speed at the mid-plane temperature, Ω the Keplerian angular velocity, Σ the surface density of the disk, and G the gravitational constant.

We adopted the surface density and the temperature at the mid-plane as a function of the radius of our best fit model. The stability condition ($Q > 1$) is satisfied up to a radius $R_{\rm disk} \sim 100$ au. A similar result has been found by Maud et al. (2019) in the massive O-type protostar

G17.64+0.16, who reported a massive and stable disk for $R_{\rm disk} \leq 150$ au. Furthermore, Meyer et al. (2018) and Takahashi et al. (2016) propose an update of the Toomre criterion in which the only necessary condition for disk instability is Q<0.6.

In addition, our best fit model satisfies the conditions proposed by Forgan et al. (2016) in order to apply the α-viscosity prescription model in self-gravitating disks; that is, $H/R < 0.1$ (see Fig. 9) and $M_{\rm disk}/M_* < 0.5$.

We note that due to the relatively high mass of the disk of our best model (5 $M_\odot$), self-gravity might play a non-negligible role. In order to explore the potential effects of including self-gravity, we compared our best fit model to the hydrodynamic simulations (including self-gravity) of massive star formation performed by Kuiper & Hosokawa (2018). Our model shows very similar results in terms of disk mid-plane temperature and disk's aspect ratio to this model (Fig. 6; Kuiper & Hosokawa 2018), which indicates that including self-gravity would not change our results significantly.

7.4. *Residual map*

The values of the residual map are low when compared with the observed (residuals are below 5% of the peak intensity), but significant with respect to the rms noise level (σ ~0.06 mJy beam^{-1}), with an intensity range between ~ 2 and −2 mJy beam^{-1} (see Fig. 6). The main differences between the observed and modeled images arise from the outer parts of the disk, beyond 150 au, with an excess and a deficit of emission. This is illustrated in Fig. 10, where we show flux density-position cuts along the major and minor axis of the disk (observed and modeled). We also verified that the asymmetries were not caused by a mismatch in the inclination of the system or a shift in the disk centers. In Fig. 11 we present the model image and the residual map of the best fit model (i=49°; central panels) together with two models in which the inclination around the best fit has been modified (i=44° and 54°). In addition, we show in Fig. 15 the χ^2 as a function of the inclination for the best fit model varying the inclination angle in a range of 10° centered at 49°.

Although we cannot discard intrinsic asymmetries within the disk, a plausible explanation for this excess/defect of emission at the outer parts of the disk could be a small mismatch with the flaring angle and/or settling of the disk. To discriminate between possible intrinsic asymmetries and modeling, we would need ALMA high-angular observations at other frequencies as it has been carried out in low-mass YSOs (e.g., Carrasco-González et al. 2019; Macías et al. 2019).

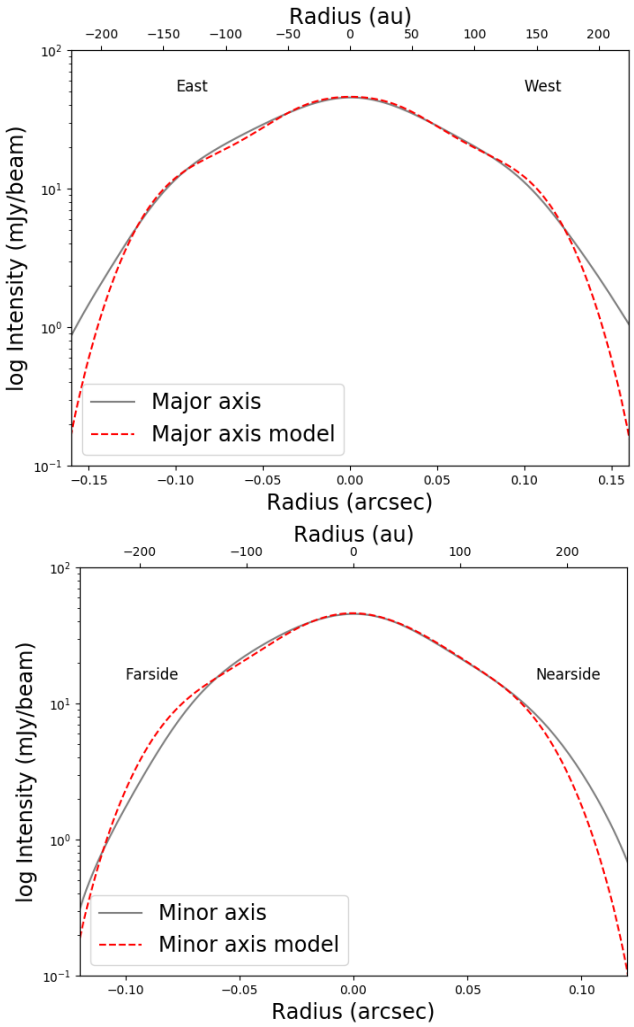


Figure 10. Cut along the major (top panel) and minor (bottom panel) axis. Solid grey and dashed red lines represent the observed image and model, respectively. The physical space scale (au) is corrected by inclination.

7.5. *Mass accretion rate and evolutionary stage*

Trinidad et al. (2003) used the D'Alessio model to fit the SED of AFGL 2591 VLA3, a massive disk-star system located in the Cygnus X region. They find that for all models, the main heating source was the stellar irradiation for radii larger than 20 au and the viscous dissipation for smaller radii. Furthermore, $\Sigma \sim \dot{M}_{\rm acc}/\alpha$ for radius larger than 20 au. In this scenario, they find a family of models that could explain the observed SED. This family of models correspond to a constant value of $\dot{M}_{\rm acc}/\alpha$, showing that the SED does not change as long as this ratio is maintained.

Our best fit model yields a rate $\dot{M}_{\rm acc}/\alpha$ ~1×10^{-4} $M_\odot$ yr^{-1}. We tested if the radial intensity profile would be significantly affected by varying the accretion rate and alpha, while keeping $\dot{M}_{\rm acc}/\alpha$ constant. As we show

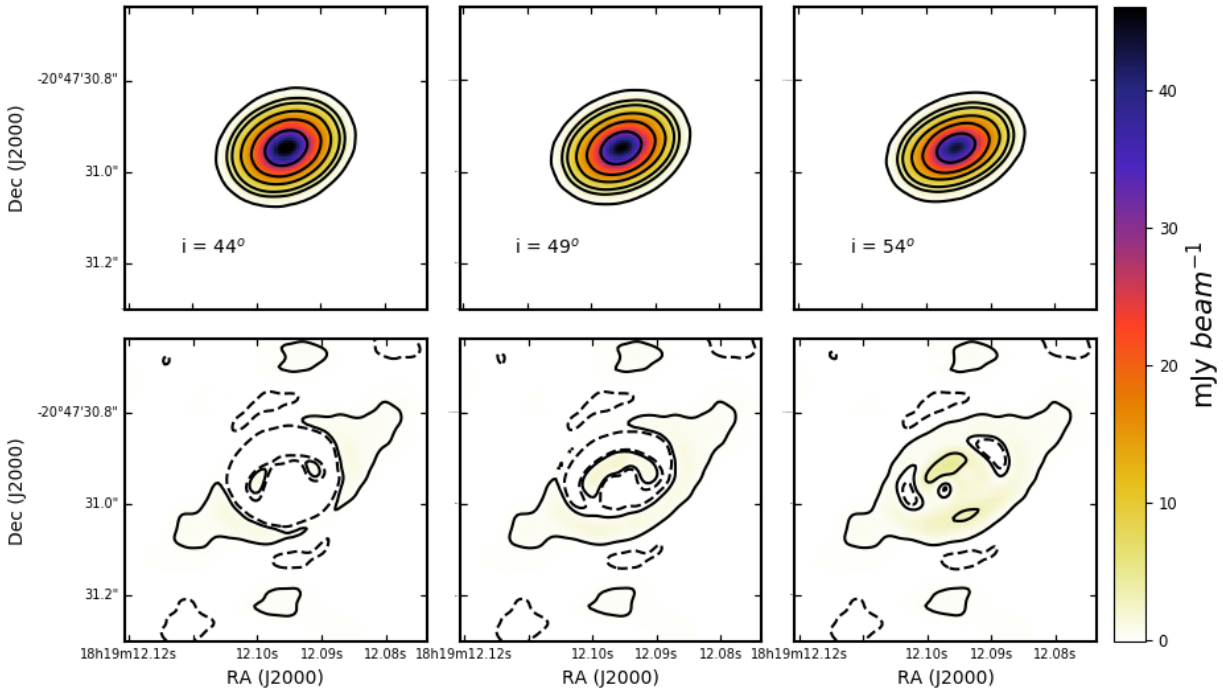


Figure 11. Models (top panels) and residuals (bottom panels) for the best fit model varying the inclination. Left panels correspond to i=44°, middle panels to i=49°, and right panels to i=54°. The contours levels are -5, 5, 50, 100, 200, 300, and 500 times the rms of the observed image (0.06 mJy beam^{-1}).

in Fig. 12, the radial intensity profile at 1.14 mm is dramatically affected when the disk mass accretion rate is changed although the ratio $\dot{M}_{\rm acc}/\alpha$ stays constant. The main reason for this difference is because of the effects of the irradiation from the accretion luminosity. Therefore by not having this degeneration we are able to constrain the $\dot{M}_{\rm acc}$.

We would like to point out that the accretion rate could be variable with time. In fact, Martí et al. (1998), based on multi-epoch VLA continuum observations, report a flux density decay of the two inner condensations in the HH 80–81 thermal radio jet. Such a flux density decay could be attributed to changes in the mass accretion rate, being higher in the past. Furthermore, GGD 27–MM1 is a young source that has a faint envelope and probably an incipient (hyper-compact) H II region. Some studies estimate that the timescale for the development of H II regions, with an accretion rate in the range $\sim 10^{-4}$–10^{-3} $M_\odot$ yr^{-1}, is $\sim 10^5$ years (e.g., Osorio et al. 1999; Cesaroni 2005). Considering the constant accretion rate of our best fit model (7×10^{-5} $M_\odot$ yr^{-1}), for it to reach a star mass of 25 $M_\odot$, its age would be $\sim 4\times10^5$ yr, which is larger than the development time of an H II region. Thus, higher accretion episodes in the past are necessary to explain the present situation.

The GGD 27 complex includes two compact cores, MM1 and MM2, separated by ∼7" (∼ 10000 au). Fernández-López et al. (2011a) estimated masses of MM1 and MM2 at different scales (see their Table 6). These authors show that while in MM2 most of the mass (∼75%) is found at envelope scale, in MM1 ∼70% of the mass is already at disk scale. This fact would place MM1 in a more evolved stadium than MM2, being MM1 equivalent to a Class I low-mass star.

7.6. *Temperature distribution in the GGD 27-MM1 disk: comparison with disks around low- and intermediate- mass stars and implications on the water snow line*

In flared α-irradiated disk models, the temperature varies as a function of both the radial distance to the star and the height above the disk mid-plane. The mid-plane temperature decreases with increasing radius, typically as $T_c \propto R^{[-0.5,-1]}$ (e.g., D'Alessio et al. 1998). In the GGD 27-MM1 disk we found $T_c \propto R^{-1}$ (see Section 6).

Furthermore, because of the flared morphology of the disk, its surface is heated directly by the radiation from the star and the accretion shock, while the inner layers are heated by viscous dissipation, which heats mainly the disk mid-plane. The energy released by the star and the accretion shock generally exceeds the one released by viscous dissipation. As a result of these heating mechanisms, the surface of the disk is warmer than the regions closer to the mid-plane, but the temperature gradient becomes smoother, or even reversed (temper-

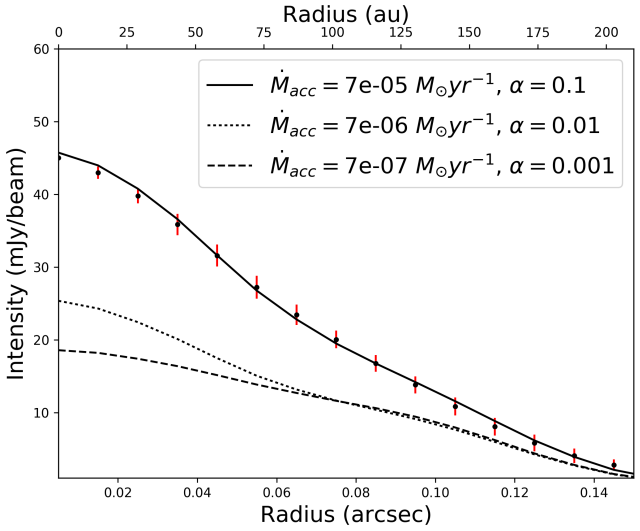


Figure 12. Averaged radial intensity profile of the best fit model (R_*=25 $R_\odot$, M_*=20 $M_\odot$, $R_{\rm disk}$=170 au, i=49°, $T_{\rm eff}$=12000 K, distance=1.4 *kpc*, $R_{\rm in}$=14 au, a_{max} 500 μm) varying $\dot{M}_{\rm acc}$and α. Solid line: Disk mass accretion rate $7{\times}10^{-5}$ $M_\odot$ yr^{-1}, α=0.1, $M_{\rm disk}$=5 $M_\odot$. Dotted line: Disk mass accretion rate $7{\times}10^{-6}$ $M_\odot$ yr^{-1}, α=0.01, $M_{\rm disk}$=8 $M_\odot$. Dashed line: Disk mass accretion rate $7{\times}10^{-7}$ $M_\odot$ yr^{-1}, α=0.001, $M_{\rm disk}$=9 $M_\odot$.

ature increasing with decreasing height), near the mid-plane. In the latter case, the minimum temperature is not reached at the mid-plane but above it.

For disks in low-mass stars this vertical inversion only happens typically at radii $\leq$ 1 au and heights $\leq$ 1 au (D'Alessio et al. 1997, 1998). According to our modeling, in the case of the GGD 27–MM1 disk the vertical inversion of temperature occurs at all radii; for instance, near the star, at $R_{\rm disk} \simeq$ 30 au, the inversion occurs at a height of $\sim$ 5 au and at a temperature of $\sim$ 240 K, while in the outermost regions, $R_{\rm disk} \simeq$ 150 au, the inversion occurs at a height of $\sim$ 30 au and at a temperature of $\sim$120 K.

Typical disks around low-mass stars reach very low temperatures ($\sim$ 20–30 K at $\sim$ 150 au; D'Alessio et al. 1997; Men'shchikov et al. 1999; Fogel et al. 2011; Tobin et al. 2018). Disks around intermediate-mass stars have slightly higher values of the minimum temperature ($\sim$ 30–40 K at $\sim$ 150 au; Osorio et al. 2014). In contrast, according to our modeling, the GGD 27–MM1 disk is significantly warmer. Even at large distances from the star, close to the edge of the disk ($R_{\rm disk} \simeq$ 170 au), its mid-plane temperature remains above $\sim$140 K (see Fig. 9) and at this radius the minimum temperature is $\sim$ 115 K at a height of $\sim$ 30 au. High temperatures have also been reported for disk candidates around other massive protostars (mid-plane $T_c \simeq$ 200 K at $R_{\rm disk} \simeq$ 200 au; Chen et al. 2016), using radiative transfer models which take into account radial and vertical temperature gradients. However in most cases, the temperatures have been inferred from vertically isothermal models that do not provide the temperature of the surface layer; also, it is unclear if some of the disk candidates are indeed real accretion disks or just elongated structures, since they are extremely large.

Due to the elevated temperatures of GGD 27–MM1 disk, condensation fronts, known as snow lines, of major volatile such as carbon monoxide, carbon dioxide and methane, are not expected to be present since these species sublimate at temperatures considerably lower ($\sim$ 20–40 K, Zhang et al. 2015) than the temperatures we find in the GGD 27–MM1 disk. Nevertheless, water ice sublimates at temperatures above 100 K, hence it is possible that the water snow line is present in the outer regions of GGD 27–MM1 disk. Since the water ice sublimation temperature depends on the density (e.g., Sandford & Allamandola 1993; Osorio et al. 2009), taking into account the density and temperature distributions obtained in our modeling of the GGD 27–MM1 disk (see Section 6), we estimate that the water snow line would be located near the edge of the disk, at a radius of $\sim$ 170 au. At this radius, densities are 1×10^9–2×10^{11} cm^{-3} within a height of 30 au of the mid-plane, implying a range of water sublimation temperatures of 120–130 K, which is similar to the range of temperatures of $\sim$ 120–150 K predicted by our model.

It has been thought that water snow lines are important because they can trigger the growth of grains to pebbles and lastly to planets. They are also important because they mark the border between rocky planets formed inward of this line and giant gas planets formed outside. In the case of the GGD 27–MM1 disk, we expect the formation of gas planets to be hindered by the high temperatures of the disk, being restricted to radii near the disk edge. Consequently, we speculate that if the formation of gas planets were to occur in disks around massive protostars, in general, they would be formed at distances around hundreds of au. It is unclear, however, whether such giant planets could survive after the onset of an H II region around the massive star.

One should keep in mind that the planetary formation process in high-mass protostars, if it takes place, must be fast because the time scales for the formation of these stars are shorter than for low-mass stars. In principle, the time scale for planet formation is expected to be of the order of that of mass exchange in the accretion disk, roughly estimated as the disk mass divided by the accretion rate, resulting in 7×10^4 yr for the disk of GGD 27–MM1. This time scale is shorter than the values typically estimated for the grain coagulation

process ($\sim 10^6$ yr, Testi et al. 2014), required for particles to become cores and eventually planetesimals ending in planets. However, some additional factors should be also taken into account: (i) the full disk lifetime is larger than the time scale of mass exchange in the disk, resulting in more available time for the final planetary mass to be assembled. In particular, in the GGD 27–MM1 disk, where infall is still significant, the disk is still being replenished with new material from the surrounding envelope that makes its life longer; (ii) at later stages, hydrodynamic models show that the accretion of material onto planet embryos can largely exceed the accretion onto the star itself (Zhu et al. 2011), speeding up the planet formation; (iii) the density of particles in massive disks is much higher than in low-mass disks. Thus, the density of planetesimals would be higher and one would expect planet assembling to be faster than in the low-mass case, analogously to what happens in the formation of the star itself, which is a faster process for high-mass stars; (iv) lastly, for low-mass stars there is both theoretical (Lambrechts & Johansen 2012) and observational evidence (HL Tau: Carrasco-González et al. 2016; TMC 1A: Harsono et al. 2018) suggesting that planet formation starts very early in the star-formation process. These results imply that the planetary formation process might be faster than initially thought and compatible with the time scales of massive star-formation.

Obtaining observational constraints on the location of the water snow line in the GGD 27–MM1 disk would be of major importance to inform about the plausibility of gas planet formation around this massive protostar. We note that in low-mass protostars, water snow lines are difficult to detect because they are commonly located at very small distances, of only a few au, from the star, requiring a very high angular resolution to detect them. Cieza et al. (2016) observed V883 Ori during an outburst, when an increase in luminosity drove the water snow line out to more than 40 au ($\sim 0.1''$ at the distance of Orion), making the detection feasible. Since in the GGD 27–MM1 disk the water snow line is expected to be located at a radius of $\sim$ 170 au, resulting in a similar angular separation, $\sim 0.1''$, at the distance of GGD 27–MM1, it would not require of a stellar outburst, as in the case of low-mass protostars, to become detectable. High angular resolution ALMA observations of the GGD 27–MM1 disk at several frequencies could help to constrain the presence of the water snow line by looking for spatial variations of the dust optical depth (e.g., Cieza et al. 2016).

8. CONCLUSIONS

We used ALMA continuum observations at 1.14 mm, obtained with an angular resolution of $\sim$40 mas, to model the accretion disk around the central massive early B-type protostar exciting the powerful HH 80–81 radio jet using α-viscosity prescription. We found an enclosed mass of 21–30 $M_\odot$, of which 5–7 $M_\odot$ can be attributed to the disk. This mass is consistent with the derived dynamical mass of 31 ± 1 $M_\odot$ and 21 ± 1 $M_\odot$ for the SO_2 $9_{2,8}$–$8_{1,7}$ and $19_{3,17}$–$19_{2,18}$ lines, respectively. The radius of the disk is $\sim$170 au, with an inclination angle of 49°. We compared the physical structure, temperature and density profiles, obtained with our model with power law functions, showing that the GGD 27–MM1 system is a potential template for future similar studies in other high-mass protostars. In particular, we obtained a flared disk with a maximum scale height of $\sim$13 au, and a temperature profile that ranges from $\sim$150 K at the outskirts of the disk up to $\sim$1400 K at the inner edge of the disk. The analysis of the Toomre Q parameter, evaluated at the disk mid-plane temperature, indicates that the disk is stable up to a radius $R_{\rm disk} \simeq$100 au. This work shows that the D'Alessio models can be used as a first approximation in the modeling of accretion disks around massive protostars, providing in addition several observational predictions.

We also reported the presence of an unresolved compact source at the center of the accretion disk, with a radius of 4 mas ($\sim$5.6 au at the source distance of 1.4 kpc) and a brightness temperature of $\sim 10^4$ K, most likely tracing ionized gas. The origin of this compact source is uncertain, it could arise from an incipient, extremely compact H II region or from the base of the HH 80–81 radio jet. Observations at higher angular resolution would help to determine the nature of this compact source.

Finally, we have estimated a distance of 1.2-1.4 kpc to the GGD 27 star-forming region based on the Gaia DR2 catalogue combined with near-IR polarimetric data of the YSOs in the region and the extinction maps.

ACKNOWLEDGMENTS

We are grateful to Nuria Calvet for making D'Alessio's code available to us and for very useful discussions. We would also like to deeply thank Guillem Anglada for his critical comments on this work that have undoubtedly improved it very substantially. We thank our anonymous referee for her/his very helpful comments and suggestions to improve our manuscript. We also thank Rosine Lallement for the support on *STILISM*. This paper makes use of the following ALMA data: ADS/JAO.ALMA#2015.1.00480.S. ALMA is a

partnership of ESO (representing its member states), NSF (USA) and NINS (Japan), together with NRC (Canada) and NSC and ASIAA (Taiwan) and KASI (Republic of Korea), in cooperation with the Republic of Chile. The Joint ALMA Observatory is operated by ESO, AUI/NRAO and NAOJ. This work has made use of data from the European Space Agency (ESA) mission *Gaia* (https://www.cosmos.esa.int/gaia), processed by the *Gaia* Data Processing and Analysis Consortium (DPAC, https://www.cosmos.esa.int/web/gaia/dpac/consortium). Funding for the DPAC has been provided by national institutions, in particular the institutions participating in the *Gaia* Multilateral Agreement. N. A.-L, M.O., J.M.G,G.B., R.E., and J.M.T. are supported by the Spanish grant AYA2017-84390-C2-R (AEI/FEDER, UE). R.E. is also supported by MDM-2014-0369 of ICCUB (Unidad de Excelencia "María de Maeztu"). M.O. acknowledges financial support from the State Agency for Research of the Spanish MCIU through the "Center of Excellence Severo Ochoa" award for the Instituto de Astrofísica de Andalucía (SEV-2017-0709). S.C. acknowledges support from DGAPA, UNAM and CONACyT, México. M.F-L. acknowledges support from the LACEGAL project which has received funding from the European Union's Horizon 2020 Research an Innovation Program under the Marie Sklodowska-Curie grant agreement No 734374. R.G.M. acknowledges support from UNAM PAPIIT project IN 104319. J.K. is supported by MEXT KAKENHI grant number 19K14755.

Software: CASA (McMullin et al. 2007), MIRIAD (Sault et al. 1995), PYTHON, STILISM

APPENDIX

A. THE DISTANCE TO THE LDN 291 CLOUD

The GGD 27 nebulosity and the objects associated to the region (e.g., HH 80-81, and the HH 80N star forming core Heathcote et al. 1998; Girart et al. 1994, 2001; Masqué et al. 2011, 2013) are located in the LDN 291 large molecular cloud complex (including the dark clouds LDN 306, 314, 315 and 322) that extends $\sim 4^\circ$ in Sagittarius (Lynds 1962; Reipurth et al. 2008; Saito et al. 1999). The distances reported in the literature range between 1.5 and 2.4 kpc (e.g. Racine 1968; Humphreys 1978; Rodriguez et al. 1980). However, the most used value in the literature is 1.7 kpc. For this distance, the spatial scale of LDN 291 cloud complex is $\sim$75 pc $\times$19 pc and the mass is $\sim$1.2 10^5 $M_\odot$ (Saito et al. 1999).

A.1. *Analysis*

Here we present two different approaches to better estimate the distance to the LDN 291 / GGD 27 region. The two approaches rely on the Gaia DR2 catalogue (Gaia Collaboration et al. 2016, 2018). First, we used data from Gaia in combination with near-IR polarimetric data of the YSOs located in the GGD 27 region (Kwon et al. 2016). The second approach is to use the on-line *STILISM*[1] application (Capitanio et al. 2017; Lallement et al. 2018), which combines the Gaia data with extinction maps to obtain 3-D dust maps of the Galaxy.

A.1.1. *Method 1: Young Stellar Objects in GGD 27 and Gaia*

Figure 13 shows the polarization fraction as a function of the Gaia DR2 parallax for the YSOs in GGD 27 (from the Kwon et al. (2016) and This figure shows that the YSOs population with counterpart in GAIA have distances clearly smaller than the distance adopted in the literature, 1.7 kpc. Most of the YSOs have parallaxes between $\sim$0.6 mas (1.67 kpc) and 1.2 mas (830 pc) but with significant uncertainties. However, there are two objects that have large parallaxes. One of them is [HL85] GGD 27-28 31 (Hartigan & Lada 1985). It is located at a distance of 362 ± 58 pc but has very high polarization levels (26%, 42% and 57% in the JHK bands, respectively; Kwon et al. 2016). This star is located in front of the bright GGD 27 nebula, where high levels of circular polarization are detected. Therefore, the near-IR linear polarization is likely coming from the nebula and it is not related with the optical star. The other star, 2MASS J18185959-2045537, is located at 395 ± 31 pc and it exhibits no polarization in the near-IR, which indicates that this is a (cold) foreground star not related to the cloud. In order to estimate the distance we calculated for the

[1] https://stilism.obspm.fr

YSOs the average value of the Gaia parallaxes weighted with the uncertainty:

$$< \pi_{\rm GGD27} >= \frac{\sum_i^N \pi_i/\sigma_i^2}{\sum_i^N 1/\sigma_i^2} \tag{A1}$$

and the uncertainty is:

$$\sigma(< \pi >) = \sqrt{\frac{N}{\sum_i^N 1/\sigma_i^2}} \tag{A2}$$

π_i and σ_i are the parallax for each star and its uncertainty, respectively, from the GAIA DR2 catalogue. We excluded four stars with parallaxes, within their uncertainties, larger than 0.9 mas (with distances less than ≃1100 pc). Using the rest of the sample, we obtain an average, weighted by the uncertainty, parallax of 0.801 ± 0.106 mas. Therefore, the distance to the YSO cluster is 1248±166 pc.

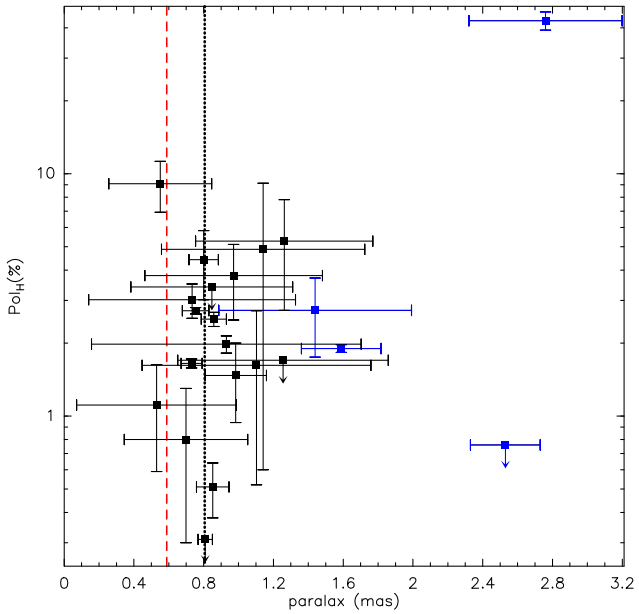


Figure 13. Gaia parallax (in mas) *versus* polarization fraction in the H band for the YSO stars that appear in any of the Kwon et al. (2016) and Qiu & Zhang (2009) catalogues. The blue color stars have distances smaller than ≃1100 pc (considering their error bars), suggesting that they are not associated with the cloud. These stars were not used in the cloud distances estimation. The black dashed vertical line shows the averaged parallax (weighted by the uncertainty) of the YSOs in GGD 27, 0.81 mas (1.25 kpc). The red dashed vertical line shows the parallax for the distance previously adopted in the literature, 1.7 kpc.

A.1.2. *Method 2: Extinction-Gaia data – STILISM*

A recent work (Danielski et al. 2018) has correlated the Gaia distances and the corrected version of G extinction with archival ground based data, specially with 2MASS and SDSS/APOGEA-DR14 (Capitanio et al. 2017; Lallement et al. 2018). This allows to derive 3D maps of the extinction as a function of the distance. We used the on-line tool that provides the cumulative reddening curve as a function of the distance for a given line-of-sight. Figure 14 shows the $E(B-V)$ extinction as a function of the distance toward the LDN 291 / GGD 27 region. It clearly shows two abrupt increases of the extinction, a small one ($E(B-V)$ ∼0.2 mag or $A_{\rm V}$ ∼0.6 mag) around 100 pc and a larger one ($E(B-V)$ ∼0.7 mag or $A_{\rm V}$ ∼2.0 mag) around 1200 pc. In order to fit the two abrupt extinction jumps, we used the following approach:

$$E(B-V) = \frac{A_0}{1+e^{-A_1(D-D_{\rm jump})}} + A_2 D + A_3, \tag{A3}$$

where D is the distance, $D_{\rm jump}$ is the distance where the jump occurs and A_i (i = 0, ..., 3) are free parameters. We used a reduced χ^2 fit. The distance for the large jump is 1270 ± 65 pc. We also used this expression to estimate the first small extinction jump, obtaining a distance of 119 ± 15 pc.

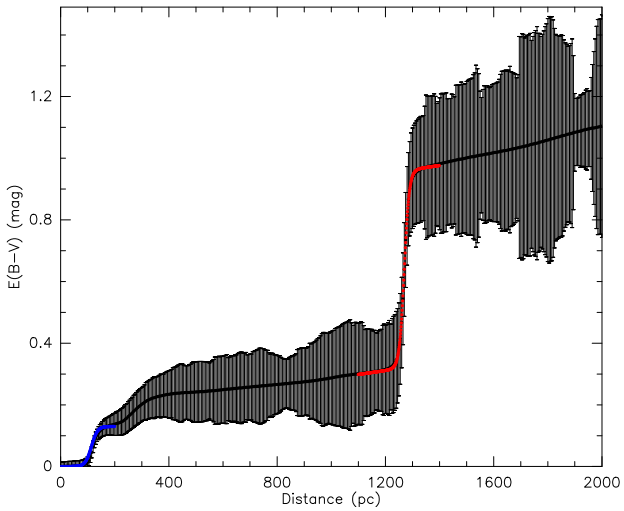


Figure 14. $E(B-V)$ extinction (in magnitudes) as a function of the distance toward the GGD 27 region obtained from the *STILISM* (Structuring by Inversion the Local Interstellar Medium) on-line application (Capitanio et al. 2017; Lallement et al. 2018). The blue and red lines are the fit to the visual extinction jump at 119 and 1270 pc, respectively.

A.1.3. *Distance to the GGD 27 nebula/molecular cloud*

The YSOs detected with Gaia are likely near the surface of the cloud, otherwise the cloud extinction would make them not visible at optical wavelengths. Indeed, most of the *Spitzer* YSOs from Qiu & Zhang (2009) do not have optical counterparts. The previous analysis indicates that the average distance within 1-σ uncertainty is between ∼1100 to 1400 pc. The second method is even more very sensitive to the cloud's surface, giving a distance between 1200 and 1340 pc (also at 1 σ level). Therefore, combining both methods, we can constrain the distance to the GGD 27 region in the range of 1200 to 1400 pc.

B. MODEL ROBUSTNESS

As we already advanced in Section 5, Figure 15 shows how the χ^2 value changes when we vary the main parameters of the disk, while fixing the others to the best fit value. The same scale for the Y-axis (χ^2) is used in the four panels. The parameters under study were varied between ∼ 10% and ∼ 30% according to the observational restrictions (see Section 4). The four parameters show a minimum at the value of our best fit model. The panel shows that the model is much more sensitive to changes in inclination and disk radius, where the parameter variations are around 10%, compared to changes in the inner radius and accretion rate, where the variations are over 30%.

Regarding the inner radius, we situated the sublimation wall at 12 au (± 2 au), based on the luminosity and the dust sublimation temperature. Inward from this border the dust can not survive, thus we can not obtain a physically consistent model with an inner radius smaller than 14 au. In addition, an inner radius larger than ∼20 au (∼14 mas) is discarded because it should have been observed with the angular resolution of our ALMA observations.

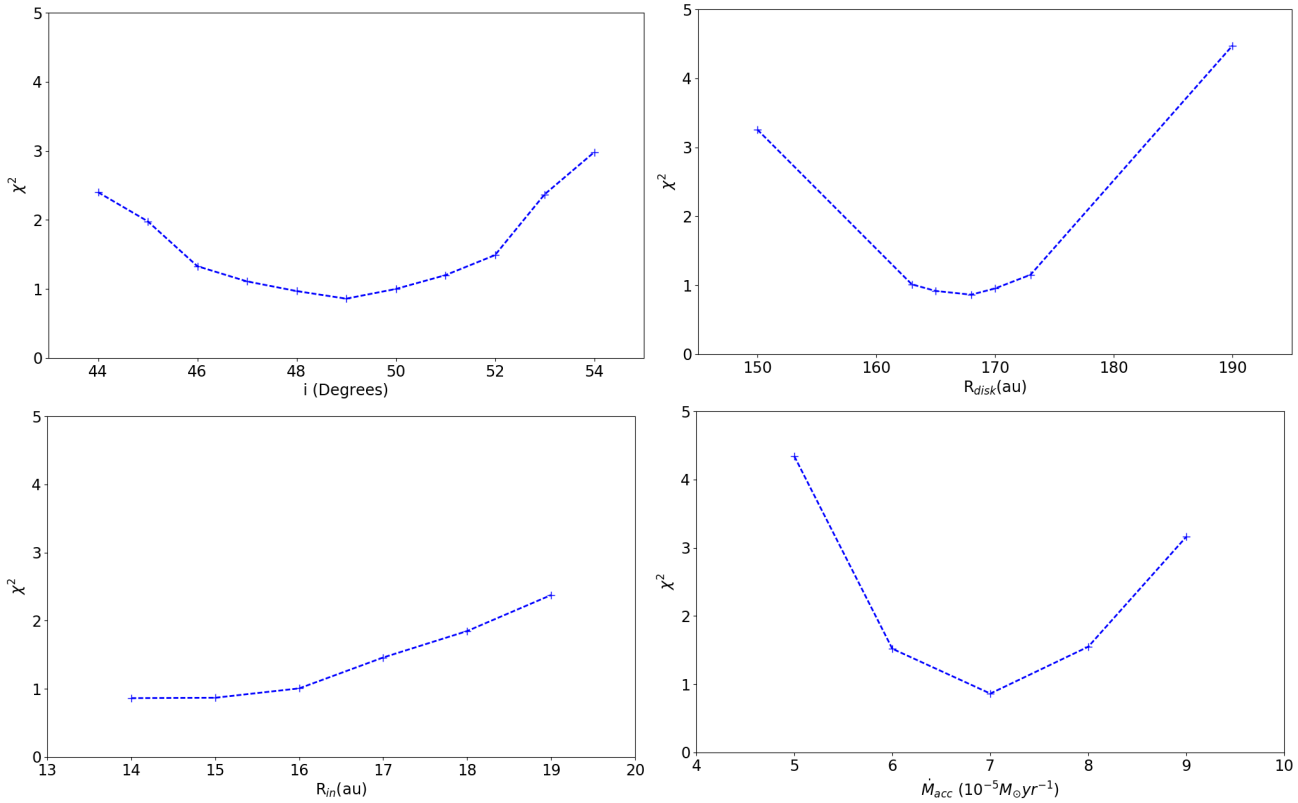


Figure 15. χ^2 **for the best fit model varying inclination (upper left),** $\mathbf{R_{disk}}$ **(upper right),** $\mathbf{R_{in}}$ **(bottom left),** $\dot{M}_{\rm acc}$**(bottom right).**

REFERENCES

Andrews, S. M., Huang, J., Pérez, L. M., et al. 2018, ApJ, 869, L41

Anglada, G., Rodríguez, L. F., & Carrasco-González, C. 2018, A&A Rv, 26, 3

Beltrán, M. T., Cesaroni, R., Neri, R., & Codella, C. 2011, A&A, 525, A151

Beltrán, M. T., & de Wit, W. J. 2016, A&A Rv, 24, 6

Beltrán, M. T., Sánchez-Monge, Á., Cesaroni, R., et al. 2014, A&A, 571, A52

Bontemps, S., Andre, P., Terebey, S., & Cabrit, S. 1996, A&A, 311, 858

Busquet, G., Girart, J. M., Estalella, R., et al. 2019, A&A, 623, L8

Capitanio, L., Lallement, R., Vergely, J. L., Elyajouri, M., & Monreal-Ibero, A. 2017, A&A, 606, A65

Carrasco-González, C., Rodríguez, L. F., Anglada, G., et al. 2010, Science, 330, 1209

Carrasco-González, C., Galván-Madrid, R., Anglada, G., et al. 2012, ApJL, 752, L29

Carrasco-González, C., Henning, T., Chand ler, C. J., et al. 2016, ApJL, 821, L16

Carrasco-González, C., Sierra, A., Flock, M., et al. 2019, ApJ, 883, 71

Cesaroni, R. 2005, in IAU Symposium, Vol. 227, Massive Star Birth: A Crossroads of Astrophysics, ed. R. Cesaroni, M. Felli, E. Churchwell, & M. Walmsley, 59–69

Chen, H.-R. V., Keto, E., Zhang, Q., et al. 2016, ApJ, 823, 125

Cieza, L. A., Casassus, S., Tobin, J., et al. 2016, Nature, 535, 258

D'Alessio, P., Calvet, N., & Hartmann, L. 1997, ApJ, 474, 397

—. 2001, ApJ, 553, 321

D'Alessio, P., Calvet, N., Hartmann, L., Franco-Hernández, R., & Servín, H. 2006, ApJ, 638, 314

D'Alessio, P., Calvet, N., Hartmann, L., Lizano, S., & Cantó, J. 1999, ApJ, 527, 893

D'Alessio, P., Cantö, J., Calvet, N., & Lizano, S. 1998, ApJ, 500, 411

Danielski, C., Babusiaux, C., Ruiz-Dern, L., Sartoretti, P., & Arenou, F. 2018, A&A, 614, A19

De Buizer, J. M., Osorio, M., & Calvet, N. 2005, ApJ, 635, 452

Draine, B. T., & Lee, H. M. 1984, ApJ, 285, 89

Dullemond, C. P., & Dominik, C. 2004, in Astronomical Society of the Pacific Conference Series, Vol. 321, Extrasolar Planets: Today and Tomorrow, ed. J. Beaulieu, A. Lecavelier Des Etangs, & C. Terquem, 361

Fernández-López, M., Curiel, S., Girart, J. M., et al. 2011a, AJ, 141, 72

Fernández-López, M., Girart, J. M., Curiel, S., et al. 2011b, AJ, 142, 97

Fogel, J. K. J., Bethell, T. J., Bergin, E. A., Calvet, N., & Semenov, D. 2011, ApJ, 726, 29

Forgan, D. H., Ilee, J. D., Cyganowski, C. J., Brogan, C. L., & Hunter, T. R. 2016, MNRAS, 463, 957

Gaia Collaboration, Prusti, T., de Bruijne, J. H. J., et al. 2016, A&A, 595, A1

Gaia Collaboration, Brown, A. G. A., Vallenari, A., et al. 2018, A&A, 616, A1

Ginsburg, A., McGuire, B., Plambeck, R., et al. 2019, ApJ, 872, 54

Girart, J. M., Estalella, R., Viti, S., Williams, D. A., & Ho, P. T. P. 2001, ApJL, 562, L91

Girart, J. M., Rodriiguez, L. F., Anglada, G., et al. 1994, ApJL, 435, L145

Girart, J. M., Estalella, R., Fernández-López, M., et al. 2017, ApJ, 847, 58

Girart, J. M., Fernández-López, M., Li, Z.-Y., et al. 2018, ApJL, 856, L27

Gómez, Y., Rodríguez, L. F., Girart, J. M., Garay, G., & Martí, J. 2003, ApJ, 597, 414

Harsono, D., Bjerkeli, P., van der Wiel, M. H. D., et al. 2018, Nature Astronomy, 2, 646

Hartigan, P., & Lada, C. J. 1985, ApJS, 59, 383

Hartmann, L., Herczeg, G., & Calvet, N. 2016, ARA&A, 54, 135

Heathcote, S., Reipurth, B., & Raga, A. C. 1998, AJ, 116, 1940

Hosokawa, T., & Omukai, K. 2009, ApJ, 691, 823

Humphreys, R. M. 1978, ApJS, 38, 309

Ilee, J. D., Cyganowski, C. J., Brogan, C. L., et al. 2018, ApJL, 869, L24

Johnston, K. G., Shepherd, D. S., Robitaille, T. P., & Wood, K. 2013, A&A, 551, A43

Johnston, K. G., Robitaille, T. P., Beuther, H., et al. 2015, ApJL, 813, L19

Klassen, M., Pudritz, R. E., Kuiper, R., Peters, T., & Banerjee, R. 2016, ApJ, 823, 28

Kuiper, R., & Hosokawa, T. 2018, A&A, 616, A101

Kwon, J., Tamura, M., Hough, J. H., et al. 2016, ApJ, 824, 95

Lallement, R., Capitanio, L., Ruiz-Dern, L., et al. 2018, A&A, 616, A132

Lambrechts, M., & Johansen, A. 2012, A&A, 544, A32

Lynds, B. T. 1962, ApJS, 7, 1

Macías, E., Espaillat, C. C., Ribas, Á., et al. 2018, ApJ, 865, 37
Macías, E., Espaillat, C. C., Osorio, M., et al. 2019, ApJ, 881, 159
Martí, J., Rodríguez, L. F., & Reipurth, B. 1993, ApJ, 416, 208
Martí, J., Rodríguez, L. F., & Reipurth, B. 1998, ApJ, 502, 337
Masqué, J. M., Girart, J. M., Anglada, G., et al. 2013, ApJ, 776, 28
Masqué, J. M., Osorio, M., Girart, J. M., et al. 2011, ApJ, 738, 43
Masqué, J. M., Rodríguez, L. F., Araudo, A., et al. 2015, ApJ, 814, 44
Maud, L. T., Cesaroni, R., Kumar, M. S. N., et al. 2019, A&A, 627, L6
McClure, M. K., D'Alessio, P., Calvet, N., et al. 2013, ApJ, 775, 114
McKee, C. F., & Ostriker, E. C. 2007, ARA&A, 45, 565
McMullin, J. P., Waters, B., Schiebel, D., Young, W., & Golap, K. 2007, in Astronomical Society of the Pacific Conference Series, Vol. 376, Astronomical Data Analysis Software and Systems XVI, ed. R. A. Shaw, F. Hill, & D. J. Bell, 127
Men'shchikov, A. B., Henning, T., & Fischer, O. 1999, ApJ, 519, 257
Meyer, D. M. A., Kuiper, R., Kley, W., Johnston, K. G., & Vorobyov, E. 2018, MNRAS, 473, 3615
Motogi, K., Hirota, T., Machida, M. N., et al. 2019, ApJL, 877, L25
Osorio, M., Anglada, G., Lizano, S., & D'Alessio, P. 2009, ApJ, 694, 29
Osorio, M., Lizano, S., & D'Alessio, P. 1999, ApJ, 525, 808
Osorio, M., Anglada, G., Carrasco-González, C., et al. 2014, ApJL, 791, L36
Osorio, M., Macías, E., Anglada, G., et al. 2016, ApJL, 825, L10
Patel, N. A., Curiel, S., Sridharan, T. K., et al. 2005, Nature, 437, 109
Qiu, K., Wyrowski, F., Menten, K., Zhang, Q., & Güsten, R. 2019, ApJ, 871, 141
Qiu, K., & Zhang, Q. 2009, ApJ, 702, L66
Racine, R. 1968, AJ, 73, 233
Reipurth, B., Rodney, S. A., & Heathcote, S. 2008, Star Formation in Sagittarius: The Lynds 291 Cloud, ed. B. Reipurth, 578
Reynolds, S. P. 1986, ApJ, 304, 713
Rodriguez, L. F., Moran, J. M., Ho, P. T. P., & Gottlieb, E. W. 1980, ApJ, 235, 845
Rodríguez-Kamenetzky, A., Carrasco-González, C., Araudo, A., et al. 2017, ApJ, 851, 16
Saito, H., Tachihara, K., Onishi, T., et al. 1999, PASJ, 51, 819
Sánchez-Monge, Á., Beltrán, M. T., Cesaroni, R., et al. 2014, A&A, 569, A11
Sandford, S. A., & Allamandola, L. J. 1993, ApJ, 417, 815
Sanna, A., Moscadelli, L., Goddi, C., Krishnan, V., & Massi, F. 2018, A&A, 619, A107
Sault, R. J., Teuben, P. J., & Wright, M. C. H. 1995, in Astronomical Society of the Pacific Conference Series, Vol. 77, Astronomical Data Analysis Software and Systems IV, ed. R. A. Shaw, H. E. Payne, & J. J. E. Hayes, 433
Seifried, D., Sánchez-Monge, Á., Walch, S., & Banerjee, R. 2016, MNRAS, 459, 1892
Shakura, N. I., & Sunyaev, R. A. 1973, A&A, 500, 33
Shu, F. H., Lizano, S., & Adams, F. C. 1987, in IAU Symposium, Vol. 115, Star Forming Regions, ed. M. Peimbert & J. Jugaku, 417–433
Takahashi, S. Z., Tsukamoto, Y., & Inutsuka, S. 2016, MNRAS, 458, 3597
Tan, J. C., Beltrán, M. T., Caselli, P., et al. 2014, in Protostars and Planets VI, ed. H. Beuther, R. S. Klessen, C. P. Dullemond, & T. Henning, 149
Testi, L., Birnstiel, T., Ricci, L., et al. 2014, Protostars and Planets VI, 339
Tobin, J. J., Looney, L. W., Li, Z.-Y., et al. 2018, ApJ, 867, 43
Trinidad, M. A., Curiel, S., Cantó, J., et al. 2003, ApJ, 589, 386
Williams, J. P., & Cieza, L. A. 2011, ARA&A, 49, 67
Yang, H., Li, Z.-Y., Looney, L. W., Girart, J. M., & Stephens, I. W. 2017, MNRAS, 472, 373
Zapata, L. A., Garay, G., Palau, A., et al. 2019, ApJ, 872, 176
Zhang, K., Blake, G. A., & Bergin, E. A. 2015, ApJL, 806, L7
Zhu, Z., Nelson, R. P., Hartmann, L., Espaillat, C., & Calvet, N. 2011, ApJ, 729, 47